remote sensing

MDPI

Review

Imaging Spectroscopy for Methane Point-Source Detection and Quantification: Methods, Applications, and Perspectives

Zhipeng Pei [1,2], Ge Han [1,2,*], Huiqin Mao [3], Cuihong Chen [3], Jun Wang [4] and Wei Gong [5]

1 School of Remote Sensing and Information Engineering, Wuhan University, Wuhan 430072, China; zhipeng.pei@whu.edu.cn
2 Perception and Effectiveness Assessment for Carbon-Neutrality Efforts, Engineering Research Center, Ministry of Education, Institute for Carbon Neutrality, Wuhan University, Wuhan 430079, China
3 Center for Satellite Applications on Ecology and Environment, Ministry of Ecology and Environment, Beijing 100094, China; maohq@secmep.cn (H.M.); chench@secmep.cn (C.C.)
4 International Institute for Earth System Science, Nanjing University, Nanjing 210023, China; wangjun@nju.edu.cn
5 State Key Laboratory of Information Engineering in Surveying, Mapping, and Remote Sensing, Wuhan University, Wuhan 430079, China; weigong@whu.edu.cn
* Correspondence: udhan@whu.edu.cn

Abstract

High-resolution imaging spectroscopy has enabled the detection and quantification of methane emissions from individual facilities, providing valuable information for identifying large emission sources and evaluating emission inventories. This review synthesizes research on broad-spectrum imaging spectrometers through an end-to-end framework linking spectral characterization, methane enhancement retrieval, plume segmentation and emission-rate estimation. We first review atmospheric radiative transfer and spectral characterization, followed by methane enhancement retrieval methods, including IMAP-DOAS, matched filters, and their variants. We then discuss the identification of methane plumes, with particular attention to false-positive suppression and recent developments in automated plume segmentation. Emission-rate estimation methods, including Gaussian plume inversion, cross-sectional flux, integrated mass enhancement, and machine learning approaches, are compared in terms of their underlying assumptions and sources of uncertainty. We also examine the probability of detection and emission persistence, which are essential for interpreting nondetections and estimating emissions from repeated observations. Applications across oil and gas infrastructure, coal mines, landfills, offshore facilities, and accidental releases demonstrate the capability of imaging spectroscopy to identify major emission sources and reveal their spatial and temporal variability. Continued advances in spectral calibration, methane enhancement retrieval, automated plume identification, and emission-rate estimation, together with coordinated multisensor observations, will further improve the accuracy, consistency, and temporal coverage of facility-scale methane monitoring.

Keywords: methane; imaging spectroscopy; point-source emissions

Check for updates

Academic Editor: Christoffer Karoff

Received: 12 October 2026
Revised: 2 November 2026
Accepted: 3 November 2026
Published: 6 November 2026

Copyright: © 2026 by the authors. Licensee MDPI, Basel, Switzerland. This article is an open access article distributed under the terms and conditions of the Creative Commons Attribution (CC BY) license.

1. Introduction

Methane (CH_4) is the second-largest contributor to anthropogenic greenhouse-gas radiative forcing after carbon dioxide (CO_2). Its strong radiative effect and relatively short atmospheric lifetime make emission reductions particularly crucial for limiting near-term warming [1–3]. Yet atmospheric methane continues an unrelenting upward trajectory,

with the World Meteorological Organization reporting a globally averaged surface mole fraction of 1948 ppb in 2025, approximately 167% above pre-industrial levels [4]. This sustained rise unfolds against a complex background of natural and anthropogenic sources whose spatial and temporal distributions vary dramatically. Wetlands and inland waters drive broadly distributed natural emissions modulated by temperature and moisture cycles, whereas anthropogenic fluxes span everything from dispersed agricultural activities and waste management to highly concentrated point sources in fossil-fuel extraction and transport infrastructure. These industrial releases can be sustained operational leaks or intermittent, high-rate venting and equipment malfunctions, creating a heterogeneous landscape of sources that demands diverse observational strategies [5–8].

To untangle this heterogeneity, monitoring frameworks have evolved across complementary spatial and temporal scales. Regional atmospheric observations and large-scale flux inversions constrain continental and national budgets, but resolving individual emitters requires high-resolution imaging spectroscopy and targeted facility-scale measurements [9–11]. Such data can provide an independent evaluation of emission inventories, which are typically estimated using reported activity data and emission factors [12]. Airborne surveys have underscored the heavy-tailed distribution of point-source emissions across oil, gas, and industrial infrastructure, revealing that a small fraction of facilities contributes disproportionately to total regional output [5–7]. Frequent observations to determine whether these super-emitters are persistent or intermittent are essential for developing accurate emission inventories and implementing targeted mitigation measures [13].

Satellite remote sensing of methane relies on measurements of solar radiation reflected by the Earth's surface and modified by atmospheric absorption. Imaging spectrometers record this radiation in hundreds of contiguous spectral channels, allowing methane abundance to be retrieved from its absorption features in the shortwave infrared (SWIR), particularly near 1650 and 2300 nm. Early satellite missions, including SCIAMACHY, GOSAT, and TROPOMI, established accurate methane column measurements for regional and global emission monitoring [9,14–16]. Among these instruments, TROPOMI combines a high spectral resolution of approximately 0.25 nm in the SWIR with a 2600-km swath, enabling daily global coverage. However, its relatively coarse spatial resolution of 7×5.5 km^2 limits the detection and attribution of individual methane plumes [17]. Figure 1 compares methane plumes observed by instruments with different spatial resolutions.

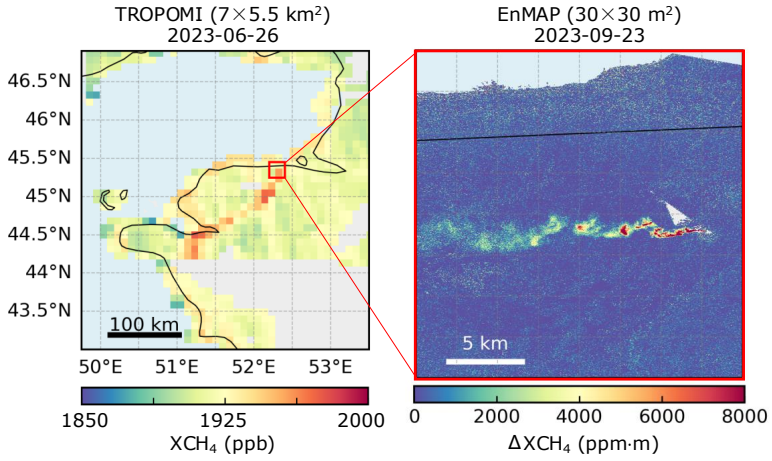


Figure 1. Comparison of regional methane observations from TROPOMI on 26 June 2023 and facility-scale methane plume observations from EnMAP on 23 September 2023 near 45.3324°N, 52.3730°E in Kazakhstan. TROPOMI shows column-averaged methane concentrations, whereas EnMAP shows methane enhancements relative to the local background. The observations illustrate the different spatial scales resolved by the two instruments and were not acquired simultaneously.

Recent advances in imaging spectroscopy have enabled methane plumes to be mapped at much finer spatial scales [5,10]. High-resolution methane imaging instruments can be broadly divided into two categories according to their spectral coverage. The first comprises broad-spectrum imaging spectrometers that sample a wide spectral range, typically from approximately 400 to 2500 nm. These instruments generally have spectral sampling intervals of the order of 5–10 nm, but offer spatial resolutions of tens of metres from space and as fine as a few metres from airborne platforms. In terms of imaging geometry, imaging spectrometers commonly employ either whiskbroom or pushbroom scanning. Most contemporary spaceborne imaging spectrometers adopt pushbroom designs, which acquire an entire across-track line simultaneously and build a three-dimensional hyperspectral data cube through successive acquisitions along the satellite's flight path, as illustrated in Figure 2. This design allows longer detector integration times and avoids mechanical cross-track scanning, improving signal-to-noise performance and instrument stability [18]. Representative spaceborne instruments include PRISMA [19], EnMAP [20], EMIT [21], GF-5A/B AHSI [22], and ZY-1E/F AHSI [23]. The Tanager satellites, developed by Planet Labs in collaboration with the nonprofit Carbon Mapper initiative, also belong to this category [24]. Methane retrievals from these instruments typically exploit the absorption features near 2300 nm. Although their spectral resolution is substantially coarser than that of dedicated atmospheric composition sensors, their finer spatial sampling reduces the dilution of localized plumes within individual pixels, allowing methane enhancements to produce detectable changes in the measured radiances.

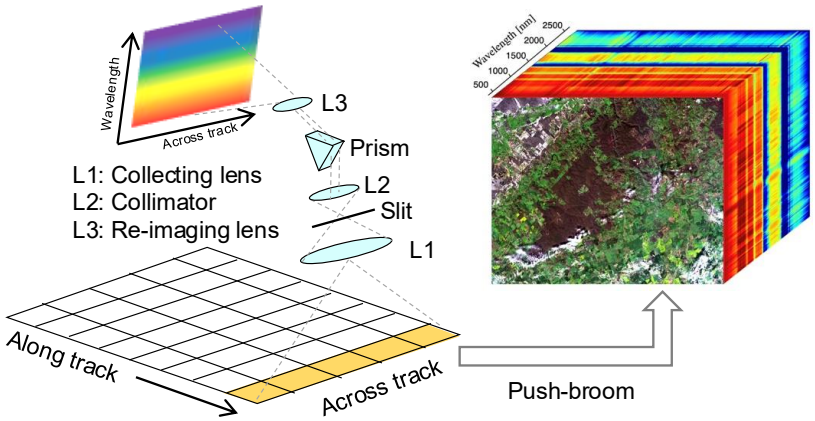


Figure 2. Schematic illustration of a pushbroom imaging spectrometer and the acquisition of a hyperspectral data cube. A cross-track line is imaged through the optical system and spectrally dispersed onto a two-dimensional detector array. As the satellite moves along its flight path, successive acquisitions are combined to form a three-dimensional data cube containing two spatial dimensions and one spectral dimension.

The second category comprises methane-focused imaging spectrometers that measure a narrower spectral window around the 1650-nm methane absorption band, typically with sub-nanometre spectral resolution. Examples include the GHGSat constellation [25,26] and MethaneSAT, developed by the Environmental Defense Fund [27]. GHGSat employs targeted staring observations to obtain methane measurements at approximately 25-m spatial resolution over relatively small scenes [25]. Its observations are primarily tasked over selected sites for industrial, governmental, and other monitoring applications. Unlike data from conventional open-access satellite missions, GHGSat data are not unrestrictedly available, although approved research access is provided through dedicated programmes. MethaneSAT, in contrast, was designed for basin-scale methane monitoring, combining a 200-km swath with 100×400 m^2 spatial sampling and high-precision methane measurements. Its instrument had a spectral resolution of 0.25 nm and a spectral sampling interval

of 0.08 nm in the methane absorption window. The MethaneSAT mission operated from March 2024 until June 2025 [27].

In addition to these imaging spectrometers, multispectral missions such as Sentinel-2, Landsat, and WorldView-3 have demonstrated the capability to detect and quantify strong methane plumes using their SWIR bands [28–32]. These instruments provide additional opportunities for methane monitoring through their spatial resolution, revisit frequency, and existing image archives.

This review specifically focuses on methane point-source detection and quantification using broad-spectrum imaging spectrometers. By combining high spatial resolution with contiguous SWIR spectral coverage, these instruments enable the mapping of localized methane plumes and the attribution of concentration enhancements to individual facilities. Translating these radiance measurements into reliable emission estimates involves spectral characterization, methane enhancement retrieval, plume segmentation, and emission-rate estimation, as illustrated in Figure 3. By reviewing these processing stages, we identify and discuss the key challenges to reliable methane point-source monitoring.

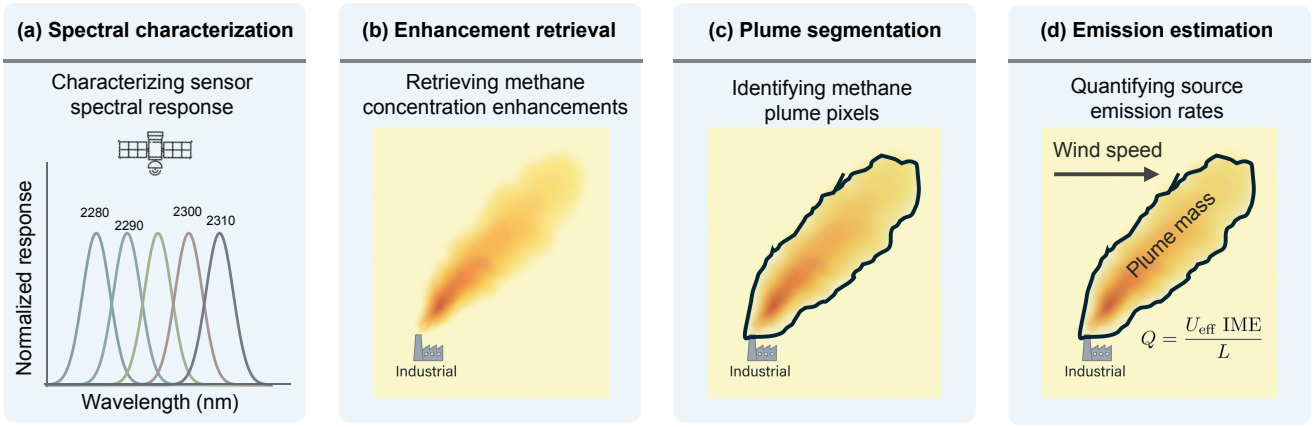


Figure 3. Schematic overview of the four main processing stages for methane point-source detection and quantification using imaging spectroscopy. (**a**) Spectral characterization determines the instrument spectral response functions. (**b**) Enhancement retrieval derives spatial distributions of methane concentration enhancements from measured radiances. (**c**) Plume segmentation identifies methane plume pixels and delineates plume boundaries. (**d**) Emission estimation converts the retrieved plume enhancements into source emission rates using wind information and quantitative estimation methods, with the integrated mass enhancement (IME) method shown as an example.

2. Atmospheric Radiative Transfer

Imaging spectrometers detect methane through its wavelength-dependent absorption of sunlight reflected by the Earth's surface. Although atmospheric radiative transfer involves both absorption and scattering, scattering is often neglected in simplified SWIR radiative transfer calculations, where Rayleigh scattering is relatively weak. Assuming a plane-parallel atmosphere and a Lambertian surface, the top-of-atmosphere (TOA) spectral radiance can be approximated as

$$L_{\text{TOA}}(\lambda) \simeq \frac{E_0(\lambda)\,\rho(\lambda)\cos\theta_s}{\pi} \times \exp\left[-(\sec\theta_s + \sec\theta_v)\sum_g \sum_l N_{g,l}\,\sigma_g(\lambda; p_l, T_l)\right], \quad (1)$$

where E_0 is the extraterrestrial solar spectral irradiance, ρ is the surface reflectance, and θ_s and θ_v are the solar and viewing zenith angles, respectively. The terms $N_{g,l}$ and σ_g denote the vertical column amount and absorption cross-section of gas g in atmospheric layer l,

respectively. The absorption cross-section depends on the pressure p_l and temperature T_l of each atmospheric layer. This expression combines surface reflection with the Beer–Lambert description of absorption along the downward and upward atmospheric paths.

For broad-spectrum imaging spectrometers, methane retrievals primarily exploit the structured absorption features near 2300 nm. In this spectral region, CH_4 absorption features overlap with those of other atmospheric constituents, particularly H_2O and N_2O, as illustrated in Figure 4. A local enhancement in methane concentration increases the atmospheric optical depth, thereby reducing the measured radiance at methane-sensitive wavelengths relative to the surrounding background. Radiative transfer models, such as libRadtran, can be used to simulate high-spectral-resolution top-of-atmosphere (TOA) radiance spectra for different methane column abundances. For a given imaging spectrometer, the radiance measured in each spectral channel is obtained by integrating the high-resolution TOA spectrum over the instrument's spectral response function (SRF):

$$L_b = \int R_b(\lambda)\, L_{\mathrm{TOA}}(\lambda)\, \mathrm{d}\lambda, \qquad \int R_b(\lambda)\, \mathrm{d}\lambda = 1, \tag{2}$$

where R_b is the normalized SRF of spectral channel b. The SRF is commonly approximated by a Gaussian function characterized by its center wavelength (CWL) and full width at half maximum (FWHM). These parameters determine how atmospheric absorption features are sampled and represented in the measured spectra.

Figure 5 illustrates the simulated TOA radiance spectra for two column-averaged methane abundances (1.8 and 2.8 ppm), obtained using libRadtran and convolved with Gaussian SRFs constructed from the nominal CWLs and FWHMs of PRISMA [33].

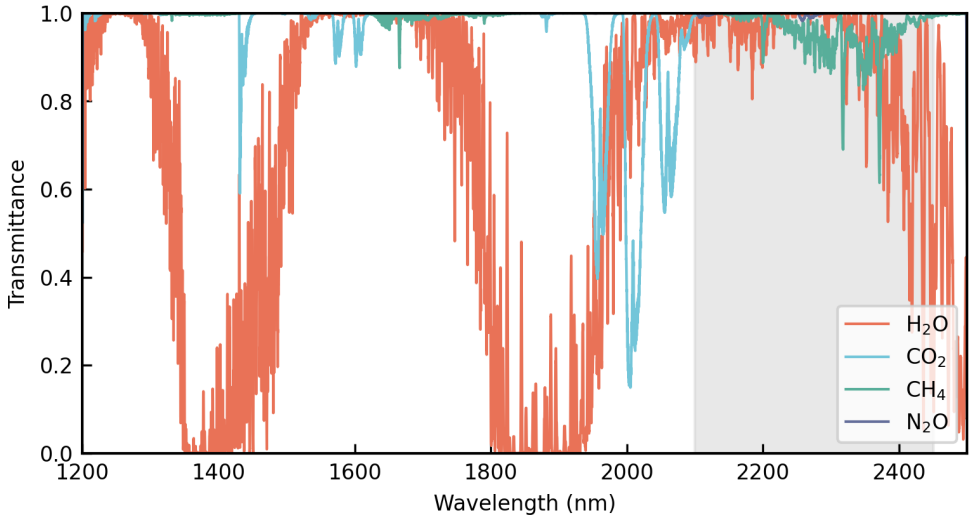


Figure 4. Vertical one-way atmospheric transmittance spectra of H_2O, CO_2, CH_4, and N_2O across 1200–2500 nm. The shaded gray areas represent the methane retrieval windows commonly used. The spectra were calculated using the HITRAN Application Programming Interface (HAPI) and the HITRAN spectroscopic database under atmospheric conditions defined by the US Standard Atmosphere 1976 (US76), with a spectral sampling interval of 0.01 cm^{-1} [34,35]. For visualization, the transmittance spectra were smoothed using a 40-point moving average.

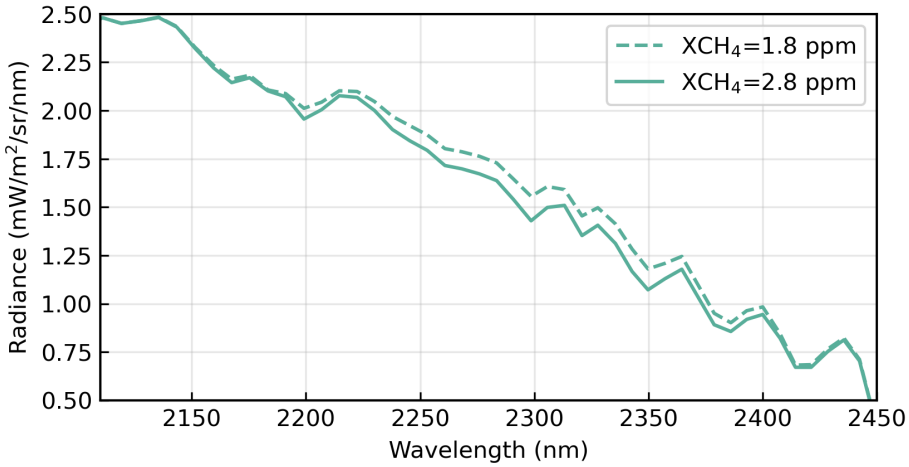


Figure 5. Simulated TOA radiance spectra for column-averaged methane abundances of 1.8 and 2.8 ppm, convolved with the nominal spectral responses of PRISMA. The simulations were performed using libRadtran with a solar zenith angle of 30°, nadir viewing, and a surface albedo of 0.3. Atmospheric profiles for other gases were taken from the US 1976 Standard Atmosphere.

3. Spectral Characterization

Although the nominal center wavelengths (CWLs) and full widths at half maximum (FWHMs) are typically determined through pre-launch laboratory calibration, these parameters may differ from their actual values during in-orbit observations. Spectral smile can cause systematic variations in CWL across the field of view, while variations in spectral bandwidth and instrumental drift may further affect the spectral response. Such deviations can lead to discrepancies between the observed absorption features and those simulated using nominal spectral parameters [36,37].

Pixel-wise algorithms such as Iterative maximum a posteriori differential optical absorption spectroscopy (IMAP-DOAS) incorporate wavelength shifts into the state vector and estimate them during the optimization process. In contrast, spectral calibration prior to methane retrieval is often omitted in applications of column-wise algorithms. Pei et al. [38] evaluated the impact of CWL and FWHM errors on column-wise methane retrievals. Their quantitative assessment showed that methane emission estimates could be systematically underestimated by up to 37% under severe combined CWL and FWHM miscalibration.

In-orbit spectral calibration of imaging spectrometers can be broadly classified into two approaches, namely onboard calibration and scene-based calibration. The former relies on onboard calibration systems, which typically include internal spectral reference sources and diffusers [39]. However, some imaging spectrometers are not equipped with dedicated onboard calibration systems due to constraints on instrument cost and simple design [40]. Scene-based approaches provide an alternative means of evaluating and characterizing the spectral performance of different instruments.

Scene-based spectral characterization has been widely adopted due to its low hardware requirements and cost-effectiveness, making it an important complementary approach for calibration and validation. These methods use Earth-reflected solar radiation and exploit atmospheric absorption features in selected spectral windows as references. By fitting radiative transfer simulations to observed spectra, scene-based spectral characterization can estimate deviations in the CWLs and FWHMs of individual spectral channels from their nominal values [37,38].

4. Methane Enhancement Retrieval

Methane enhancement retrieval translates the spectral effect of additional atmospheric methane into a spatial map of column enhancements, ΔX_{CH_4}, relative to the local background. Methods used with broad-spectrum imaging spectrometers can be broadly grouped into pixel-wise methods and column-wise methods [41]. Their primary differences lie in how they characterize atmospheric absorption and in their computational costs.

4.1. IMAP-DOAS

IMAP-DOAS is a physically based retrieval method that estimates atmospheric gas abundances by fitting simulated spectra to individual pixel observations [42–44]. The forward model uses the Beer–Lambert law to describe atmospheric absorption and a low-order polynomial to represent slowly varying spectral features associated with surface reflectance and atmospheric scattering. The high-resolution TOA radiance can be expressed as

$$F^h(\boldsymbol{x}, \lambda) = I_0(\lambda) \exp\left(-A \sum_{g=1}^{G} s_g \sum_{l=1}^{L} \tau_{g,l}(\lambda) \right) \sum_{k=0}^{K} a_k P_k(\lambda), \tag{3}$$

where $I_0(\lambda)$ is the solar irradiance spectrum, A is the geometric air mass factor, and s_g is the scaling factor applied to gas g. The term $\tau_{g,l}$ represents the vertical optical depth of gas g in atmospheric layer l, calculated from atmospheric profiles and molecular spectroscopic data. The terms P_k and a_k denote the polynomial basis functions and their corresponding coefficients, respectively. The state vector $\boldsymbol{x}$ consists of the gas scaling factors and polynomial coefficients, with wavelength shifts optionally included to account for spectral calibration uncertainties. For methane retrievals, CH_4, H_2O, and N_2O are commonly included in the forward model.

The high-resolution radiance is subsequently convolved with the instrument SRF to obtain the simulated radiance spectrum $\boldsymbol{F}(\boldsymbol{x})$. The optimal state vector is estimated by minimizing a cost function that combines the spectral fitting residuals with prior constraints:

$$\hat{\boldsymbol{x}} = \arg\min_{\boldsymbol{x}} \left[\left(\boldsymbol{y} - \boldsymbol{F}(\boldsymbol{x})\right)^T \boldsymbol{S}_\epsilon^{-1} \left(\boldsymbol{y} - \boldsymbol{F}(\boldsymbol{x})\right) + \left(\boldsymbol{x} - \boldsymbol{x}_a\right)^T \boldsymbol{S}_a^{-1} \left(\boldsymbol{x} - \boldsymbol{x}_a\right) \right], \tag{4}$$

where $\arg\min_{\boldsymbol{x}}$ denotes the value of the state vector $\boldsymbol{x}$ that minimizes the expression in brackets, $\boldsymbol{y}$ is the observed radiance spectrum, $\boldsymbol{x}_a$ is the prior state vector, and $\boldsymbol{S}_\epsilon$ and $\boldsymbol{S}_a$ are the observation and prior error covariance matrices, respectively.

By explicitly modeling atmospheric absorption and fitting each pixel independently, IMAP-DOAS is less dependent on the availability of spectrally similar background pixels than scene-statistical methods. However, its accuracy is affected by uncertainties in atmospheric conditions, surface reflectance, and spectral calibration. The iterative optimization also requires repeated forward-model evaluations, resulting in substantially higher computational costs than column-wise retrieval methods [41,45]. Since IMAP-DOAS retrieves methane column abundances, the local background must subsequently be subtracted to derive the methane enhancements associated with point-source plumes.

4.2. Matched Filter and Its Variants

Unlike IMAP-DOAS, the matched filter (MF) does not require full atmospheric radiative transfer simulations for each pixel, making it particularly advantageous for the rapid processing of large imaging spectroscopy datasets [5,46]. Conventional MF assumes that plume-free radiance spectra follow a multivariate Gaussian distribution characterized by a

mean spectrum $\boldsymbol{\mu}$ and covariance matrix $\boldsymbol{\Sigma}$. Under a first-order approximation of methane absorption, the enhancement $\alpha \equiv \Delta X_{CH_4}$ is estimated as

$$\widehat{\alpha}_{\mathrm{MF}} = \frac{\boldsymbol{t}^{\mathrm{T}}\boldsymbol{\Sigma}^{-1}(\boldsymbol{\mu} - \boldsymbol{y})}{\boldsymbol{t}^{\mathrm{T}}\boldsymbol{\Sigma}^{-1}\boldsymbol{t}}, \qquad \boldsymbol{t} = \boldsymbol{\mu} \odot \boldsymbol{k}, \tag{5}$$

where $\boldsymbol{y}$ is the observed radiance spectrum, $\boldsymbol{k}$ is the effective unit methane absorption spectrum, and $\odot$ denotes elementwise multiplication. The background statistics are commonly estimated from neighboring pixels, often separately for each detector column to accommodate cross-track radiometric differences.

The computational efficiency of MF has supported widespread application to airborne and spaceborne methane observations. Nevertheless, its accuracy depends on the validity of the linear absorption approximation and the representativeness of the background spectra. Strong methane enhancements may be underestimated, while heterogeneous surfaces, aerosols, and instrumental artifacts can produce signals resembling methane absorption [47,48]. Several variants have been developed to address these issues. MAG1C introduces sparsity-based iterative optimization to reduce background clutter [49]. MF-Combo exploits complementary spectral information from different spectral windows to suppress false methane enhancements [50]. Aerosol-calibrated MF accounts for aerosol-related effects on methane retrievals [51]. The multi-level matched filter was proposed to better distinguish background pixels from plume pixels, thereby reducing noise interference and mitigating the underestimation of strong methane enhancements [52]. Sparse spectral reconstruction has also been developed to improve retrieval performance over heterogeneous surfaces [53]. These methods address different sources of retrieval errors and contribute to more reliable methane enhancement mapping.

4.3. Lognormal Matched Filter and Its Variants

The lognormal matched filter (LMF) provides an alternative statistical formulation by assuming that background radiance follows a multivariate lognormal distribution, meaning that the logarithm of radiance follows a multivariate Gaussian distribution [54]. Under this assumption, the methane enhancement α is estimated as

$$\widehat{\alpha}_{\mathrm{LMF}} = \frac{\boldsymbol{k}^{\mathrm{T}}\boldsymbol{\Sigma}_{\mathrm{ln}}^{-1}(\boldsymbol{\mu}_{\mathrm{ln}} - \ln \boldsymbol{y})}{\boldsymbol{k}^{\mathrm{T}}\boldsymbol{\Sigma}_{\mathrm{ln}}^{-1}\boldsymbol{k}}, \tag{6}$$

where $\boldsymbol{\mu}_{\mathrm{ln}}$ and $\boldsymbol{\Sigma}_{\mathrm{ln}}$ are the mean and covariance of the log-transformed background spectra. In contrast to conventional MF, LMF does not require a first-order expansion of the assumed multiplicative methane absorption model. However, finite spectral resolution, imperfect background representation, and errors in the absorption spectrum remain sources of uncertainty.

To further reduce biases arising from plume contamination of background statistics, Pei et al. [48] proposed the iterative lognormal matched filter (ILMF). It progressively identifies methane-enhanced pixels and refines the background distribution, improving retrieval robustness when the initial background sample includes plume pixels. Together, MF, LMF, and their variants demonstrate a progression from computationally efficient spectral detection toward more reliable quantitative enhancement mapping. Nevertheless, retrieval artifacts may persist even in well-calibrated observations, motivating the plume identification and segmentation methods discussed in the following section.

5. Plume Segmentation

Methane enhancement maps derived from imaging spectrometers may contain both real methane plumes and false retrieval signals. Before estimating emission rates, false detections need to be excluded and the pixels belonging to each methane plume need to be identified. This section reviews methods for suppressing false methane enhancements and identifying plume pixels from satellite observations.

5.1. False Positive Suppression

False methane enhancements occur when retrieval algorithms report methane enhancements in pixels where no actual methane enhancement is present. One major cause is the absorption of certain surface materials, such as carbonate minerals and plastics, whose spectral features partially overlap with those of methane. At the relatively coarse spectral resolution of broad-spectrum imaging spectrometers, these surface absorption features may be incorrectly interpreted as methane absorption. False enhancements can also arise from abnormal radiance measurements and errors in the estimation of background statistics. For example, large variations in surface reflectance among pixels within the same detector column can affect the background statistics used in matched-filter retrievals and produce false methane enhancements. Instrumental effects, including spectral calibration errors and sensor noise, may further contribute to these errors [55,56]. Such retrieval errors can lead to false plume detections and affect subsequent emission-rate estimates.

Several methods have been developed to reduce false methane enhancements. Roger et al. [50] proposed MF-Combo, which combines methane retrievals from different spectral windows to reduce false signals caused by surface absorption features. Li et al. [53] introduced a sparse spectral reconstruction method to reduce false enhancements over heterogeneous surfaces. Xiang et al. [56] developed a spectroscopic method to verify candidate methane plumes by estimating atmospheric transmittance from target and background spectra. The estimated transmittance is then compared with the expected methane absorption spectrum to determine whether the detected signal is consistent with methane absorption. More recently, Bue et al. [55] proposed the Differential Matched Filter (DiffMF), which uses wavelength derivatives of whitened radiance spectra to distinguish methane absorption from spectral features that cause false enhancements. Unlike methods that examine candidate plumes after methane retrieval, DiffMF reduces false enhancement signals during the retrieval process. Although these methods can reduce false detections, removing false methane enhancements remains difficult in scenes with heterogeneous surfaces and strong variations in radiance.

5.2. Plume Identification

Methane plumes have traditionally been identified through manual interpretation of methane enhancement maps. Analysts examine the shape and spatial distribution of methane enhancements, the locations of nearby emission facilities, and the wind direction. High-resolution optical images are also used to determine whether the detected enhancements follow roads, field boundaries, or other surface features. A strong spatial correspondence between methane enhancements and surface structures often indicates retrieval artifacts rather than actual methane plumes [48,56]. Although manual interpretation can identify many false detections, it requires experienced analysts and becomes increasingly time-consuming when processing large numbers of satellite images. Automated methods based on concentration thresholds and connected pixels can identify plume regions, but their performance is sensitive to retrieval noise and the choice of threshold.

In recent years, deep learning methods have been increasingly applied to automated methane plume detection and segmentation. Joyce et al. [57] developed a deep neu-

ral network to detect methane plumes and estimate emission rates from PRISMA observations. Růžička et al. [58] investigated semantic segmentation of methane plumes using imaging spectroscopy data. Other studies have developed automated plume detection methods using multispectral satellite observations. For example, U-Plume uses a U-Net architecture for plume segmentation and emission quantification [59], while CH4Net was developed to identify methane super-emitters from Sentinel-2 imagery [60]. Rouet-Leduc and Hulbert [61] trained a vision transformer using synthetic methane plumes added to real Sentinel-2 images. Synthetic plume data can help address the limited number of labeled methane observations available for training. However, differences between synthetic and real plumes, together with variations in surface reflectance and sensor characteristics, can affect model performance when applied to new observations.

Recently, Batchu et al. [62] introduced the Methane Analysis and Plume Localization with EMIT (MAPL-EMIT) model, which uses the full EMIT radiance spectrum as input to a vision transformer. Instead of identifying plumes from previously retrieved methane enhancement maps, MAPL-EMIT combines spectral and spatial information to retrieve methane enhancements, segment methane plumes, and estimate source locations directly from hyperspectral radiance observations. This approach allows methane retrieval and plume identification to be performed within a single deep learning model. Nevertheless, detecting weak methane plumes, reducing false positives, and applying trained models to data from different imaging spectrometers remain important challenges. Accurate identification of plume pixels is particularly important for emission-rate estimation, since errors in plume boundaries directly affect the estimated plume mass and spatial extent.

6. Emission Estimation

After methane enhancement retrieval and plume segmentation, the emission rate of a point source can be estimated from the observed plume and wind information. Most established methods relate the methane column enhancement to atmospheric transport under approximately steady emission and wind conditions. They differ mainly in how the plume is represented and how the observed enhancements are used to estimate the source rate Q [63–65]. In the following equations, $\Delta\Omega$ denotes the background-subtracted methane column enhancement expressed as mass per unit area (kg m^{-2}), converted from ΔX_{CH_4}.

6.1. Gaussian Plume Inversion

Gaussian plume inversion estimates the emission rate by fitting an atmospheric dispersion model to the observed methane enhancement map. For a continuously emitting point source under steady wind conditions, the vertically integrated Gaussian plume can be expressed as

$$\Delta\Omega(x,y) = \frac{Q}{\sqrt{2\pi}\,U\,\sigma_y(x)} \exp\left[-\frac{y^2}{2\sigma_y^2(x)}\right], \qquad x > 0, \tag{7}$$

where x and y are the downwind and crosswind distances from the source, U is the wind speed representative of plume transport, and $\sigma_y(x)$ describes the crosswind dispersion of the plume. The crosswind dispersion generally increases with downwind distance due to atmospheric turbulence. The emission rate is obtained by minimizing the difference between the modeled and observed column enhancements. Depending on the implementation, the dispersion parameters, plume direction, and background concentration may also be included in the fitting process [63,65].

Gaussian plume inversion is relatively straightforward when the observed plume has a well-defined shape and approximately follows a Gaussian distribution. However, at fine spatial scales, methane plumes often exhibit irregular structures due to turbulent

transport and may deviate substantially from the assumed Gaussian distribution. Changes in wind direction and emission rate during plume transport can also cause differences between the observed plume and the fitted model. Furthermore, the estimated emission rate depends strongly on the assumed wind speed and dispersion parameters, which may introduce additional uncertainties when the local meteorological conditions are not well characterized [63,64].

6.2. Cross-Sectional Flux and Its Light Implementation

The cross-sectional flux (CSF) method estimates emission rates based on mass conservation by integrating methane column enhancements across the plume. Assuming steady emission and wind conditions, the emission rate can be expressed as

$$Q = U \int_{y_1}^{y_2} \Delta\Omega(x, y)\, \mathrm{d}y, \tag{8}$$

where U is the wind speed perpendicular to the cross-section, and $[y_1, y_2]$ defines the integration interval across the plume. In practice, multiple cross-sections are selected at different downwind distances. For each cross-section, the integrated column enhancement, also referred to as line density, can be obtained by directly integrating the observed enhancements or fitting a Gaussian function to the crosswind distribution. The corresponding line densities are then converted to fluxes using wind information. For methane, which can be considered chemically inert over the plume transport timescale, the emission rate can be estimated by averaging or fitting the fluxes obtained from multiple cross-sections [63,65]. Using multiple cross-sections helps reduce the influence of measurement noise and local variations in the plume. However, the results remain sensitive to the selected cross-sections, background subtraction, and wind speed.

The light cross-sectional flux (LCSF) method is a simplified implementation originally developed for estimating CO_2 emissions from OCO-2 observations [65]. Unlike CSF, which calculates fluxes at multiple downwind distances, LCSF uses a single sampling region constructed from the source location and wind direction. The sampling region extends downwind from the source and covers a specified width in the crosswind direction. The observations within this region are fitted with a Gaussian function in the crosswind direction, optionally including a linear background term. The integrated Gaussian function provides the line density, which is multiplied by the wind speed to estimate the emission rate. This approach avoids the need to identify multiple plume cross-sections and fit the variation in flux along the plume. It is particularly useful for observations with limited spatial coverage, such as those from narrow-swath satellite instruments. However, its accuracy depends on the assumed wind direction, the selection of the sampling region, and how well the Gaussian function represents the observed crosswind distribution.

6.3. Integrated Mass Enhancement and Its Light Implementation

The integrated mass enhancement (IME) method estimates the source rate from the total excess methane mass in the plume and an effective residence time [5,63]. The plume mass and corresponding emission rate are expressed as

$$\mathrm{IME} = \sum_{i \in \mathcal{P}} \Delta\Omega_i A_i, \qquad Q = \frac{U_{\mathrm{eff}}}{L}\, \mathrm{IME}, \tag{9}$$

where $\mathcal{P}$ is the set of plume pixels, A_i is the area of pixel i, L is a characteristic plume length, and U_{eff} is an effective wind speed accounting for plume transport and dispersion. In the widely used formulation of Varon et al. [63], L is defined from the plume area as $L = \sqrt{A_{\mathrm{plume}}}$. Other implementations use the observed along-plume integration length,

together with a corresponding definition of wind speed [65]. These choices must be kept consistent when converting plume mass into an emission rate.

IME does not require the plume to follow a Gaussian shape and is therefore widely used for individual methane plumes observed by airborne and spaceborne imaging spectrometers. The effective wind speed is commonly estimated from meteorological winds using relationships calibrated with atmospheric transport simulations [48,63]. Its accuracy depends on the plume mask, background subtraction, wind speed, and the selected length scale. In particular, missed plume pixels can underestimate the integrated mass.

More recently, Hakkarainen et al. [66] proposed the linear integrated mass enhancement (LIME) method. Instead of calculating the IME for a single plume length, LIME evaluates the cumulative methane mass at several downwind distances. For a steady source and a long-lived gas, the cumulative IME is expected to increase approximately linearly with distance, so that

$$\mathrm{IME}(x) \simeq \frac{Q}{U}\, x, \qquad Q = U\, \frac{\mathrm{d}\,\mathrm{IME}(x)}{\mathrm{d}x}. \tag{10}$$

The emission rate is derived from the slope of a linear fit to $\mathrm{IME}(x)$ at different distances from the source. LIME therefore uses information from multiple portions of the plume rather than relying on a single integration length. However, it still requires a representative wind speed, reliable background subtraction, and sufficient plume coverage [66].

6.4. Machine Learning-Based Emission-Rate Estimation

Machine learning provides another approach to estimating methane emission rates from plume observations. Instead of applying an analytical transport equation to each observed plume, a regression model learns the relationship between plume characteristics and source rates from training data. The general form can be written as

$$\widehat{Q}_{\mathrm{ML}} = f_{\boldsymbol{\theta}}(\Delta\Omega,\, \boldsymbol{w}), \tag{11}$$

where $f_{\boldsymbol{\theta}}$ is a trained model, $\Delta\Omega$ represents the two-dimensional methane enhancement image, and $\boldsymbol{w}$ denotes optional meteorological inputs, including wind speed. The model parameters $\boldsymbol{\theta}$ are learned from plume images with known emission rates, which are often generated using large-eddy simulations and combined with realistic measurement noise.

Jongaramrungruang et al. [67] developed MethaNet, a convolutional neural network that estimates emission rates directly from high-resolution methane plume images without external wind measurements. Its approach uses plume shape and spatial concentration patterns to infer information related to emission rate and atmospheric transport. Bruno et al. [59] subsequently developed U-Plume, which first identifies plume pixels using a U-Net and then estimates source rates using either a convolutional neural network or the IME method with wind information. Joyce et al. [57] also investigated neural-network-based emission estimation using PRISMA observations. More recently, Plewa et al. [68] refined the training and evaluation of convolutional-neural-network-based emission estimation to reduce systematic biases in the predicted source rates.

Machine learning can estimate emission rates rapidly once the model has been trained and can make use of plume shapes that are not well described by simple analytical models. However, its accuracy depends on the range of emission rates, wind conditions, spatial resolutions, and noise characteristics represented in the training data.

6.5. Probability of Detection and Multisensor Persistence

The probability of detection (POD) is an important metric for evaluating the methane detection capability of imaging spectrometers. Unlike the minimum detection limit (MDL),

which represents a theoretical detection threshold under specified measurement conditions, POD describes the probability of successfully detecting a methane plume at a given emission rate. POD depends not only on the instrument characteristics, including spatial resolution and measurement precision, but also on wind speed, surface reflectance, and the retrieval and plume detection algorithms [69]. Therefore, the lowest emission rate detected by an instrument does not necessarily represent its detection capability under typical observation conditions.

POD can be determined empirically through controlled release experiments or coordinated observations with instruments of higher methane detection sensitivity. Ayasse et al. [69] used coincident observations from GAO and EMIT to characterize the POD of EMIT. They fitted a statistical model relating detection probability to emission rate, wind speed, and pixel size using a Burr cumulative distribution function:

$$P = 1 - (1 + x^2)^{-1.5}, \qquad x = \Phi_7 \frac{(Q - \Phi_1)^{\Phi_3}}{h^{\Phi_5}(U - \Phi_2)^{\Phi_6}}, \tag{12}$$

where P is the detection probability, Q is the emission rate, U is the wind speed, h is the pixel size, and Φ denotes the fitted model coefficients. Under favorable observation conditions and a wind speed of 3 $\mathrm{m\,s^{-1}}$, the 90% POD for EMIT was approximately 1060 $\mathrm{kg\,h^{-1}}$. In contrast, the theoretical MDL of 244 $\mathrm{kg\,h^{-1}}$ corresponded to a POD of only about 2%, demonstrating the difference between theoretical detection sensitivity and reliable plume detection.

Simulation-based approaches provide another means of estimating POD when controlled release observations are limited. Roger et al. [70] evaluated the detection capability of EnMAP and EMIT over offshore areas by incorporating methane plumes generated from WRF-LES simulations into real satellite radiance images. For each simulated plume, the emission rate was progressively increased until the plume was detected by a prescribed detection algorithm. By repeating this procedure for multiple plume realizations and observation conditions, they estimated emission-rate thresholds corresponding to different POD levels. Their results showed that POD varies with wind speed and methane retrieval precision, which is particularly important for offshore observations where reflected solar radiance depends strongly on the sun-glint geometry.

Beyond evaluating instrument detection capability, POD is also important for estimating the persistence of methane emissions from repeated observations. Persistence describes the fraction of observations during which an emission source is active. Traditionally, simple persistence is calculated as the frequency of detected methane plumes:

$$f^* = \frac{M}{N}, \tag{13}$$

where M is the number of observations with detected methane plumes and N is the total number of valid observations. However, this approach assumes that the absence of a detected plume indicates that the source was not emitting. This assumption becomes problematic when combining observations from instruments with different detection capabilities. A source may be detected by a more sensitive airborne instrument but remain undetected by a satellite instrument even when emissions continue.

To address this issue, Ayasse et al. [69] proposed a Bayesian multisensor persistence method that accounts for the POD of individual instruments when interpreting nondetections. The method estimates the probability that a source was emitting despite the absence of a detected plume:

$$p(\text{on} \mid \text{ND}) = \frac{[1 - \text{POD}^I(Q, U)]\, p(\text{on})}{[1 - \text{POD}^I(Q, U)]\, p(\text{on}) + \text{TNR}^I\, p(\text{off})}, \tag{14}$$

where ND denotes a nondetection, POD^I is the detection probability of instrument I for a representative emission rate Q and wind speed U, and TNR^I is the true negative rate. The terms $p(\text{on})$ and $p(\text{off})$ represent the prior probabilities that the source is emitting or not emitting, respectively. The prior probability can be estimated from previous observations using either simple persistence or a model that accounts for the temporal correlation of emission activity.

Under this framework, a nondetection is included in the persistence calculation when there is sufficient confidence that the source was not emitting. Otherwise, it is treated as inconclusive and excluded. For example, Ayasse et al. [69] reported a source with a simple persistence of 75% from previous GAO observations. A subsequent EMIT nondetection would have reduced this estimate to 60%, although the estimated POD for EMIT under those conditions was only 1%. The multisensor method therefore retained the original persistence estimate, consistent with the coincident airborne observation that confirmed continued emission. By accounting for differences in instrument detection capability, multisensor persistence methods can provide more reliable estimates of emission frequency and time-averaged source emission rates [69].

7. Applications and What They Establish

High-resolution imaging spectroscopy has been applied to methane emission monitoring across a wide range of industrial activities, including oil and gas production, coal mining, waste management, and offshore operations. These observations have enabled the identification of individual emission sources, provided independent measurements for evaluating emission inventories, and revealed substantial spatial and temporal variability in methane emissions. This section reviews representative applications and their main findings.

7.1. Oil and Gas

Oil and gas production and transportation have been major targets of methane remote sensing studies. Using TROPOMI observations, Zhang et al. [71] estimated methane emissions of 2.7 ± 0.5 Tg yr^{-1} from oil and gas activities in the Permian Basin, more than twice the estimates from existing bottom-up inventories. While TROPOMI provides regional emission estimates, high-resolution imaging spectrometers can identify the individual facilities responsible for large methane releases. Early applications of PRISMA demonstrated the capability of broad-spectrum imaging spectrometers to detect and quantify methane plumes from oil and gas facilities at approximately 30-m spatial resolution [19].

Satellite observations over western Turkmenistan provided evidence of large methane releases associated with oil production infrastructure. Irakulis-Loitxate et al. [72] combined hyperspectral and multispectral satellite observations to identify 29 methane super-emitters during 2017–2020, of which 24 were associated with inactive flares venting natural gas. These findings identified specific facilities where changes in operating practices could substantially reduce methane emissions.

Repeated observations have also revealed the intermittent nature of oil and gas methane emissions. Cusworth et al. [73] conducted an airborne imaging spectroscopy survey of the Permian Basin and identified 1100 individual emission sources observed at least three times. The average observed persistence was only 26%, indicating that many large methane sources were not continuously emitting. Sources with persistence greater than 50% accounted for only 11% of the identified high-emitting infrastructure but contributed 29% of the quantified emissions. The study also found that gathering and boosting

facilities accounted for a substantial fraction of the detected emissions, demonstrating that large methane releases are not limited to production wells. Further airborne surveys of natural gas gathering pipelines identified methane emissions associated with this infrastructure and provided measurement-based constraints on pipeline emission factors [74]. Together, these studies demonstrate the importance of facility-level source attribution and repeated observations for characterizing methane emissions across the oil and gas supply chain.

7.2. Coal Mine Methane

Coal mining is another major source of anthropogenic methane emissions [75]. Methane released during underground mining is commonly transported to the atmosphere through ventilation shafts and gas drainage systems, while surface mining can produce emissions over more extensive areas. Satellite observations have provided new constraints on coal mine methane (CMM) emissions, which are often estimated using coal production data and emission factors.

Using TROPOMI observations, Sadavarte et al. [76] estimated combined emissions of 570 ± 98 Gg yr^{-1} from six coal mines in Queensland, Australia, during 2018–2019. These mines accounted for approximately 7% of Australia's coal production but contributed an estimated $55 \pm 10\%$ of the nationally reported coal mining methane emissions. In China, Peng et al. [77] used TROPOMI observations and atmospheric inversion to estimate regional CMM emissions in Shanxi Province, finding substantial differences between satellite-derived estimates and some bottom-up inventories.

High-resolution imaging spectroscopy enables these regional emissions to be examined at the facility level. Han et al. [22] used GF-5B AHSI observations to identify 138 methane plume events associated with 82 emission sources in Shanxi during 2021–2023. The detected sources exhibited a strongly skewed emission distribution, with approximately 20% of emitters contributing 50% of the integrated plume emissions. Their results also revealed discrepancies between observed point-source emissions and existing coal mine emission inventories, particularly in northern Shanxi. These findings indicate that facility-scale measurements can help identify large emitters and improve the spatial allocation of inventory emissions.

Repeated satellite observations are important for characterizing emissions from coal mine ventilation systems. Varon et al. [78] combined 14–24 wind-rotated GHGSat observations to estimate time-averaged methane emission rates from three coal mine ventilation shafts in the United States, Australia, and China. More recently, Luo et al. [13] analyzed multitemporal hyperspectral observations from GF-5A/B and ZY-1E/F, identifying 237 methane plume events from 16 sources at 10 underground coal mines. Their analysis showed substantial temporal variability in source emission rates and demonstrated that repeated sampling can reduce uncertainty in annualized emission estimates. For the studied source population, approximately 20 usable plume observations per year provided an empirical guideline for constraining annual emissions. These studies indicate that single-pass measurements are useful for identifying large emitters, while repeated observations are needed to characterize temporal variability and estimate annual emissions.

7.3. Landfills

Landfills are important anthropogenic methane sources because organic waste decomposes under anaerobic conditions. Unlike many oil and gas facilities, landfill emissions can originate from multiple locations within a single site, including active working areas, landfill covers, and gas collection systems. High-resolution methane observations are therefore useful for identifying concentrated emission areas and assessing emissions at the facility level.

Maasakkers et al. [79] combined TROPOMI and GHGSat observations to investigate large methane emissions from landfills in Buenos Aires, Delhi, Lahore, and Mumbai. TROPOMI observations were used to identify regional methane hotspots, while GHGSat measurements located the responsible landfill facilities. The estimated landfill emission rates ranged from approximately 3 to 29 t h^{-1}. The study also found that satellite-derived city-level methane emissions were 1.4–2.6 times higher than commonly used inventory estimates, with individual landfills contributing substantial fractions of the total emissions.

A larger airborne imaging spectroscopy survey was conducted by Cusworth et al. [80], who examined hundreds of landfills across 18 states in the United States between 2016 and 2022. Significant methane point-source emissions were detected at 52% of the surveyed landfills, and many sources were observed repeatedly over periods ranging from weeks to years. These findings indicate that strong landfill methane emissions are widespread and can persist over extended periods. They also demonstrate the value of imaging spectroscopy for identifying facilities where landfill gas collection or cover management may require improvement. However, emissions measured from individual plumes must be interpreted carefully when estimating total facility emissions, since landfill methane can also escape through spatially distributed sources.

7.4. Offshore Oil and Gas

Methane monitoring over offshore oil and gas facilities presents additional challenges because water has very low reflectance in the shortwave infrared. Consequently, the radiance received by imaging spectrometers is often insufficient for detecting methane absorption features. Observations under sun-glint conditions, when sunlight is reflected toward the sensor by the sea surface, can substantially increase the measured radiance and enable offshore plume detection.

Ayasse et al. [81] conducted an airborne imaging spectroscopy survey of more than 150 offshore platforms and associated infrastructure in the Gulf of Mexico. Their observations revealed a highly skewed distribution of methane emissions, with large releases frequently associated with tanks and vent stacks. The study also found relatively high emission persistence and methane loss rates among the surveyed shallow-water facilities, providing direct measurements for a sector with limited observational coverage.

Satellite observations have further demonstrated the potential for monitoring offshore methane emissions. Irakulis-Loitxate et al. [82] used WorldView-3 and Landsat 8 observations acquired under favorable illumination conditions to detect a major methane release from an offshore platform in the Gulf of Mexico. The event lasted approximately 17 days and was estimated to release 0.04 ± 0.01 Tg of methane. More recently, Roger et al. [70] evaluated the methane plume detection capability of EnMAP and EMIT over offshore areas using simulated plumes inserted into real satellite observations. Their study showed that plume detectability depends strongly on the available radiance, spatial resolution, and wind speed. These studies demonstrate that offshore methane monitoring is feasible using optical satellite observations, although its application remains strongly constrained by illumination geometry and ocean surface conditions.

7.5. Accidental Methane Releases

Accidental releases from oil and gas infrastructure can produce exceptionally large methane emissions over periods ranging from several days to several months. Satellite observations are particularly valuable for documenting these events when ground measurements are unavailable or the affected facilities are difficult to access.

The Aliso Canyon natural gas storage well blowout in California during 2015–2016 was among the earliest demonstrations of methane point-source detection from space.

Thompson et al. [83] detected methane plumes from the event using the EO-1 Hyperion imaging spectrometer, demonstrating that satellite imaging spectroscopy could identify an individual anthropogenic methane source. Independent airborne measurements by Conley et al. [84] estimated that approximately 97,100 t of methane was released during the event.

Subsequent studies demonstrated the benefits of combining multiple satellite instruments to monitor the evolution of accidental releases. Cusworth et al. [85] combined observations from several satellite missions to characterize a gas well blowout in the Eagle Ford region of Texas in 2019, estimating total methane emissions of 4800 ± 980 t during the approximately 20-day event. More recently, Guanter et al. [86] analyzed a prolonged well blowout at the Karaturun East oil field in Kazakhstan. Using observations from multiple satellite instruments, they documented methane emissions over 205 days and estimated a total release of 131 ± 34 kt from 48 high-quality emission-rate estimates.

These studies demonstrate that satellite observations can provide quantitative information on the magnitude and duration of accidental methane releases. However, estimating the total methane mass released during an event requires more than individual plume measurements. The timing of the event, changes in emission rate, and periods without valid observations must also be considered.

7.6. International Methane Monitoring and Mitigation

The growing capability of satellite methane observations has also supported international efforts to identify and reduce large methane emissions. The United Nations Environment Programme (UNEP) established the International Methane Emissions Observatory (IMEO) to improve the availability and use of methane emission data from different measurement and reporting sources. As part of this initiative, UNEP launched the Methane Alert and Response System (MARS) at COP27 in 2022 to connect satellite methane observations with mitigation actions.

MARS combines observations from multiple satellite instruments to detect large methane emission events and identify their likely sources. Regional methane observations are used to identify emission hotspots, while higher-resolution satellite measurements can help locate individual emitting facilities. Following detection and source attribution, IMEO notifies the relevant governments and operators, who can investigate the emission source and take corrective actions. Subsequent satellite observations can then be used to assess whether emissions have continued or decreased. The associated methane observations and notifications are made available through UNEP's Eye on Methane platform.

MARS initially focused on methane emissions from the oil and gas sector and expanded its alert capabilities to coal mining and waste management in 2026. This initiative demonstrates how satellite-based methane monitoring can support practical emission mitigation beyond scientific research. However, successful mitigation still depends on the ability to identify individual sources, communicate the results to responsible operators, and obtain timely responses. Continued improvements in satellite coverage, plume detection, source attribution, and repeated observations are therefore important for supporting international methane emission monitoring and mitigation efforts [87].

8. Conclusions

High-resolution imaging spectroscopy has significantly advanced the detection and quantification of methane emissions at the facility scale. Broad-spectrum imaging spectrometers, including PRISMA, EnMAP, EMIT, and GF-5 AHSI, provide spatial resolutions of tens of metres and sufficient spectral information to identify methane absorption features in the SWIR. These capabilities enable the detection of individual methane plumes and the at-

tribution of emissions to specific facilities, complementing the regional and global methane observations provided by conventional atmospheric composition satellites. Applications across oil and gas infrastructure, coal mines, landfills, offshore facilities, and accidental releases have revealed the widespread occurrence of large methane emissions, substantial differences among individual facilities, and strong temporal variability in emission rates. These observations provide important measurements for evaluating emission inventories and identifying opportunities for emission mitigation.

Reliable emission quantification depends on the accuracy of each processing stage, from spectral characterization and methane enhancement retrieval to plume segmentation and emission-rate estimation. Accurate characterization of instrument spectral responses and background radiance is essential for reducing systematic biases in methane enhancement retrievals. Improved discrimination between methane absorption and interfering spectral features from surface materials can further enhance the reliability of plume identification, particularly over heterogeneous surfaces. Emission-rate estimation can benefit from more accurate wind information, plume delineation, and appropriate atmospheric transport models. Machine learning also offers opportunities for automated plume identification and emission estimation, with independent validation and cross-instrument evaluation supporting its application across diverse surface and meteorological conditions.

Beyond the accuracy of individual plume measurements, limited temporal sampling remains a major challenge for estimating annual methane emissions. Many industrial sources exhibit intermittent emissions, and a single satellite overpass cannot determine whether a detected emission is persistent or temporary. Furthermore, the absence of a detected plume does not necessarily indicate that a source is inactive, since detection probability depends on emission rate, wind speed, surface conditions, and instrument sensitivity. Reliable estimates of emission persistence and annual emissions therefore require repeated observations together with an appropriate characterization of the probability of detection. Combining observations from multiple satellite instruments and airborne platforms can improve temporal coverage and provide complementary measurements of individual emission sources.

Future developments should focus on improving the accuracy, consistency, and automation of methane retrieval and emission quantification across different imaging spectrometers. More accurate spectral characterization, improved suppression of false enhancements, and better characterization of local wind fields are important for reducing uncertainties in individual emission estimates. Automated methods should be evaluated using independent observations and realistic plume simulations to assess their performance under different environmental conditions. At the same time, coordinated multisensor observations and repeated measurements are needed to better characterize emission persistence and support comparisons with annual emission inventories. Initiatives such as the International Methane Emissions Observatory (IMEO) and its Methane Alert and Response System (MARS) demonstrate how satellite observations can be used to identify large emission sources and support emission mitigation. Continued progress in these areas will strengthen the role of imaging spectroscopy in facility-scale methane monitoring and independent evaluation of anthropogenic methane emissions.

Author Contributions: Conceptualization, Z.P. and G.H.; investigation, Z.P. and G.H.; literature curation, Z.P.; writing—original draft preparation, Z.P. and G.H.; writing—review and editing, Z.P., G.H., H.M., C.C., J.W. and W.G. All authors have read and agreed to the published version of the manuscript.

Funding: This research was funded by the National Key R&D Program of China (Grant No. 2024YFB3910203), the National Natural Science Foundation of China (Grant No. 42605156), and China Postdoctoral Science Foundation (Grant No. 2026M790237).

Data Availability Statement: No new data were created or analyzed in this study. Data sharing is not applicable to this article.

Acknowledgments: The authors sincerely thank the three anonymous reviewers for their valuable comments and suggestions, which helped improve the quality of this manuscript. GPT-5.6 and OpenAI Codex were used to assist with the preparation of the initial draft and English-language polishing.

Conflicts of Interest: The authors declare no conflicts of interest.

Abbreviations

The following abbreviations are used in this manuscript:

AHSI	Advanced Hyperspectral Imager
CMM	Coal mine methane
CSF	Cross-sectional flux
CWL	Center wavelength
EMIT	Earth Surface Mineral Dust Source Investigation
EnMAP	Environmental Mapping and Analysis Program
FWHM	Full width at half maximum
GAO	Global Airborne Observatory
GF	Gaofen (Chinese for "high resolution")
HAPI	HITRAN Application Programming Interface
HITRAN	High-Resolution Transmission Molecular Absorption Database
ILMF	Iterative lognormal matched filter
IMAP-DOAS	Iterative maximum a posteriori differential optical absorption spectroscopy
IME	Integrated mass enhancement
IMEO	International Methane Emissions Observatory
LCSF	Light cross-sectional flux
LES	Large-eddy simulation
LIME	Linear integrated mass enhancement
LMF	Lognormal matched filter
MARS	Methane Alert and Response System
MDL	Minimum detection limit
MF	Matched filter
POD	Probability of detection
PRISMA	PRecursore IperSpettrale della Missione Applicativa
SRF	Spectral response function
SWIR	Shortwave infrared
TNR	True-negative rate
TOA	Top of atmosphere
TROPOMI	TROPOspheric Monitoring Instrument
UNEP	United Nations Environment Programme
WRF-LES	Weather Research and Forecasting–Large-Eddy Simulation
ZY	Ziyuan (Chinese for "resources")

References

1. Masson-Delmotte, V.; Zhai, P.; Pirani, A.; Connors, S.L.; Péan, C.; Berger, S.; Caud, N.; Chen, Y.; Goldfarb, L.; Gomis, M.; et al. Climate change 2021: The physical science basis. In *Contribution of 731 Working Group I to the Sixth Assessment Report of the Intergovernmental Panel on Climate Change*; Cambridge University Press: Cambridge, UK; New York, NY, USA, 2021; Volume 2.
2. UNEP; CCAC. *Global Methane Assessment: Benefits and Costs of Mitigating Methane Emissions*; Cambridge University Press: Cambridge, UK, 2021.

3. Jackson, R.B.; Saunois, M.; Bousquet, P.; Canadell, J.G.; Poulter, B.; Stavert, A.R.; Bergamaschi, P.; Niwa, Y.; Segers, A.; Tsuruta, A. Increasing anthropogenic methane emissions arise equally from agricultural and fossil fuel sources. *Environ. Res. Lett.* **2020**, *15*, 071002. [CrossRef]
4. World Meteorological Organization. WMO Greenhouse Gas Bulletin No. 22. Available online: https://wmo.int/resources/publication-series/greenhouse-gas-bulletin/no-22 (accessed on 1 November 2026).
5. Frankenberg, C.; Thorpe, A.K.; Thompson, D.R.; Hulley, G.; Kort, E.A.; Vance, N.; Borchardt, J.; Krings, T.; Gerilowski, K.; Sweeney, C.; et al. Airborne methane remote measurements reveal heavy-tail flux distribution in Four Corners region. *Proc. Natl. Acad. Sci. USA* **2016**, *113*, 9734–9739. [CrossRef]
6. Duren, R.M.; Thorpe, A.K.; Foster, K.T.; Rafiq, T.; Hopkins, F.M.; Yadav, V.; Bue, B.D.; Thompson, D.R.; Conley, S.; Colombi, N.K.; et al. California's methane super-emitters. *Nature* **2019**, *575*, 180–184. [CrossRef]
7. Cusworth, D.H.; Thorpe, A.K.; Ayasse, A.K.; Stepp, D.; Heckler, J.; Asner, G.P.; Miller, C.E.; Yadav, V.; Chapman, J.W.; Eastwood, M.L.; et al. Strong methane point sources contribute a disproportionate fraction of total emissions across multiple basins in the United States. *Proc. Natl. Acad. Sci. USA* **2022**, *119*, e2202338119. [CrossRef]
8. Zhang, Y.; Han, G.; Huang, Y.; Wang, H.; Zhang, H.; Pei, Z.; Pu, Y.; Luo, H.; Yi, J.; Shi, T.; et al. Attributing GHG emissions to individual facilities using multi-temporal hyperspectral images: Methodology and applications. *ISPRS J. Photogramm. Remote Sens.* **2026**, *232*, 937–956. [CrossRef]
9. Jacob, D.J.; Turner, A.J.; Maasakkers, J.D.; Sheng, J.; Sun, K.; Liu, X.; Chance, K.; Aben, I.; McKeever, J.; Frankenberg, C. Satellite observations of atmospheric methane and their value for quantifying methane emissions. *Atmos. Chem. Phys.* **2016**, *16*, 14371–14396. [CrossRef]
10. Thorpe, A.K.; Roberts, D.A.; Bradley, E.S.; Funk, C.C.; Dennison, P.E.; Leifer, I. High resolution mapping of methane emissions from marine and terrestrial sources using a Cluster-Tuned Matched Filter technique and imaging spectrometry. *Remote Sens. Environ.* **2013**, *134*, 305–318. [CrossRef]
11. Huang, Y.; Han, G.; Yi, J.; Shi, T.; Zhang, Y.; Luo, H.; Mao, H.; Li, S.; Mao, F.; Gong, W. Rapid methane flux estimation combining MethaneSAT and Sentinel-5P observations: A case study of Turkmenistan. *Geophys. Res. Lett.* **2025**, *52*, e2025GL119369. [CrossRef]
12. Su, X.; Han, G.; Yue, Y.; Chen, C.; Pei, Z.; Luo, H.; Qin, K.; Gong, W. Characterizing Global Methane Point-Source Emission Structures from Multi-Source Satellite Data and National Inventories: Implications for Differentiated Mitigation Pathways. *Remote Sens.* **2026**, *18*, 1765. [CrossRef]
13. Luo, H.; Han, G.; Mao, H.; Wang, H.; Huang, Y.; Pei, Z.; Qin, K.; Yin, W.; Xu, W.; Li, M.; et al. Constraining Annual Coal Mine Methane Emissions with Multitemporal Hyperspectral Satellite Observations. *Environ. Sci. Technol.* **2026**, 60, 27718–27731. [CrossRef]
14. Frankenberg, C.; Bergamaschi, P.; Butz, A.; Houweling, S.; Meirink, J.F.; Notholt, J.; Petersen, A.K.; Schrijver, H.; Warneke, T.; Aben, I. Tropical methane emissions: A revised view from SCIAMACHY onboard ENVISAT. *Geophys. Res. Lett.* **2008**, *35*, L15811. [CrossRef]
15. Parker, R.J.; Webb, A.; Boesch, H.; Somkuti, P.; Barrio Guillo, R.; Di Noia, A.; Kalaitzi, N.; Anand, J.S.; Bergamaschi, P.; Chevallier, F.; et al. A decade of GOSAT Proxy satellite CH 4 observations. *Earth Syst. Sci. Data* **2020**, *12*, 3383–3412. [CrossRef]
16. Hu, H.; Hasekamp, O.; Butz, A.; Galli, A.; Landgraf, J.; Aan de Brugh, J.; Borsdorff, T.; Scheepmaker, R.; Aben, I. The operational methane retrieval algorithm for TROPOMI. *Atmos. Meas. Tech.* **2016**, *9*, 5423–5440. [CrossRef]
17. Veefkind, J.P.; Aben, I.; McMullan, K.; Förster, H.; de Vries, J.; Otter, G.; Claas, J.; Eskes, H.J.; de Haan, J.F.; Kleipool, Q.; et al. TROPOMI on the ESA Sentinel-5 Precursor: A GMES mission for global observations of the atmospheric composition for climate, air quality and ozone layer applications. *Remote Sens. Environ.* **2012**, *120*, 70–83. [CrossRef]
18. Guanter, L.; Kaufmann, H.; Segl, K.; Förster, S.; Rogass, C.; Chabrillat, S.; Küster, T.; Hollstein, A.; Rossner, G.; Chlebek, C.; et al. The EnMAP Spaceborne Imaging Spectroscopy Mission for Earth Observation. *Remote Sens.* **2015**, *7*, 8830–8857. [CrossRef]
19. Guanter, L.; Irakulis-Loitxate, I.; Gorroño, J.; Sánchez-García, E.; Cusworth, D.H.; Varon, D.J.; Cogliati, S.; Colombo, R. Mapping methane point emissions with the PRISMA spaceborne imaging spectrometer. *Remote Sens. Environ.* **2021**, *265*, 112671. [CrossRef]
20. Roger, J.; Irakulis-Loitxate, I.; Valverde, A.; Gorroño, J.; Chabrillat, S.; Brell, M.; Guanter, L. High-resolution methane mapping with the EnMAP satellite imaging spectroscopy mission. *IEEE Trans. Geosci. Remote Sens.* **2024**, *62*, 4102012. [CrossRef]
21. Thorpe, A.K.; Green, R.O.; Thompson, D.R.; Brodrick, P.G.; Chapman, J.W.; Elder, C.D.; Irakulis-Loitxate, I.; Cusworth, D.H.; Ayasse, A.K.; Duren, R.M.; et al. Attribution of individual methane and carbon dioxide emission sources using EMIT observations from space. *Sci. Adv.* **2023**, *9*, eadh2391. [CrossRef]
22. Han, G.; Pei, Z.; Shi, T.; Mao, H.; Li, S.; Mao, F.; Ma, X.; Zhang, X.; Gong, W. Unveiling unprecedented methane hotspots in China's leading coal production hub: A satellite mapping revelation. *Geophys. Res. Lett.* **2024**, *51*, e2024GL109065. [CrossRef]
23. Lu, T.; Li, Z.; Fan, C.; He, Z.; Jiang, X.; Zhang, Y.; Gao, Y.; Xuan, Y.; de Leeuw, G. Global Methane Retrieval, Monitoring, and Quantification in Hotspot Regions Based on AHSI/ZY-1 Satellite. *Atmosphere* **2025**, *16*, 510. [CrossRef]
24. Duren, R.M.; Cusworth, D.; Ayasse, A.; Howell, K.; Diamond, A.; Scarpelli, T.; Kim, J.; O'Neill, K.; Lai-Norling, J.; Thorpe, A.; et al. The Carbon Mapper emissions monitoring system. *Atmos. Meas. Tech.* **2025**, *18*, 6933–6958. [CrossRef]

25. Jervis, D.; McKeever, J.; Durak, B.O.; Sloan, J.J.; Gains, D.; Varon, D.J.; Ramier, A.; Strupler, M.; Tarrant, E. The GHGSat-D imaging spectrometer. *Atmos. Meas. Tech.* **2021**, *14*, 2127–2140. [CrossRef]
26. McLinden, C.A.; Griffin, D.; Davis, Z.; Hempel, C.; Smith, J.; Sioris, C.; Nassar, R.; Moeini, O.; Legault-Ouellet, E.; Malo, A. An Independent Evaluation of GHGSat Methane Emissions: Performance Assessment. *J. Geophys. Res. Atmos.* **2024**, *129*, e2023JD039906. [CrossRef]
27. Guanter, L.; Roger, J.; Warren, J.; Sargent, M.; Zhang, Z.; Roche, S.; Chan Miller, C.; Steiner, M.; Hadfield, H.; Omara, M.; et al. Surveying methane point-source super-emissions across oil and gas basins with MethaneSAT. *Atmos. Chem. Phys.* **2026**, *26*, 2941–2963. [CrossRef]
28. Varon, D.J.; Jervis, D.; McKeever, J.; Spence, I.; Gains, D.; Jacob, D.J. High-frequency monitoring of anomalous methane point sources with multispectral Sentinel-2 satellite observations. *Atmos. Meas. Tech.* **2021**, *14*, 2771–2785. [CrossRef]
29. Ehret, T.; De Truchis, A.; Mazzolini, M.; Morel, J.M.; D'aspremont, A.; Lauvaux, T.; Duren, R.; Cusworth, D.; Facciolo, G. Global tracking and quantification of oil and gas methane emissions from recurrent sentinel-2 imagery. *Environ. Sci. Technol.* **2022**, *56*, 10517–10529. [CrossRef]
30. Pandey, S.; van Nistelrooij, M.; Maasakkers, J.D.; Sutar, P.; Houweling, S.; Varon, D.J.; Tol, P.; Gains, D.; Worden, J.; Aben, I. Daily Detection and Quantification of Methane Leaks Using Sentinel-3: A Tiered Satellite Observation Approach with Sentinel-2 and Sentinel-5P. *Remote Sens. Environ.* **2023**, *296*, 113716. [CrossRef]
31. Sánchez-García, E.; Gorroño, J.; Irakulis-Loitxate, I.; Varon, D.J.; Guanter, L. Mapping methane plumes at very high spatial resolution with the WorldView-3 satellite. *Atmos. Meas. Tech.* **2022**, *15*, 1657–1674. [CrossRef]
32. Gorroño, J.; Varon, D.J.; Irakulis-Loitxate, I.; Guanter, L. Understanding the potential of Sentinel-2 for monitoring methane point emissions. *Atmos. Meas. Tech.* **2023**, *16*, 89–107. [CrossRef]
33. Emde, C.; Buras-Schnell, R.; Kylling, A.; Mayer, B.; Gasteiger, J.; Hamann, U.; Kylling, J.; Richter, B.; Pause, C.; Dowling, T.; et al. The libRadtran software package for radiative transfer calculations (version 2.0.1). *Geosci. Model Dev.* **2016**, *9*, 1647–1672. [CrossRef]
34. Gordon, I.E.; Rothman, L.S.; Hargreaves, R.J.; Hashemi, R.; Karlovets, E.V.; Skinner, F.M.; Conway, E.K.; Hill, C.; Kochanov, R.V.; Tan, Y.; et al. The HITRAN2020 molecular spectroscopic database. *J. Quant. Spectrosc. Radiat. Transf.* **2022**, *277*, 107949. [CrossRef]
35. Kochanov, R.V.; Gordon, I.E.; Rothman, L.S.; Wcisło, P.; Hill, C.; Wilzewski, J.S. HITRAN Application Programming Interface (HAPI): A comprehensive approach to working with spectroscopic data. *J. Quant. Spectrosc. Radiat. Transf.* **2016**, *177*, 15–30. [CrossRef]
36. Guanter, L.; Richter, R.; Moreno, J. Spectral calibration of hyperspectral imagery using atmospheric absorption features. *Appl. Opt.* **2006**, *45*, 2360–2370. [CrossRef]
37. Guanter, L.; Segl, K.; Sang, B.; Alonso, L.; Kaufmann, H.; Moreno, J. Scene-based spectral calibration assessment of high spectral resolution imaging spectrometers. *Opt. Express* **2009**, *17*, 11594–11606. [CrossRef]
38. Pei, Z.; Han, G.; Roger, J.; Gong, W.; Guanter, L. Scene-Based Spectral Characterization of Spaceborne Imaging Spectrometers in Different Spectral Windows. *IEEE Trans. Geosci. Remote Sens.* **2026**, *64*, 4111016. [CrossRef]
39. Storch, T.; Honold, H.P.; Chabrillat, S.; Habermeyer, M.; Tucker, P.; Brell, M.; Ohndorf, A.; Wirth, K.; Betz, M.; Kuchler, M.; et al. The EnMAP imaging spectroscopy mission towards operations. *Remote Sens. Environ.* **2023**, *294*, 113632. [CrossRef]
40. Thompson, D.R.; Green, R.O.; Bradley, C.; Brodrick, P.G.; Mahowald, N.; Dor, E.B.; Bennett, M.; Bernas, M.; Carmon, N.; Chadwick, K.D.; et al. On-orbit calibration and performance of the EMIT imaging spectrometer. *Remote Sens. Environ.* **2024**, *303*, 113986. [CrossRef]
41. Ayasse, A.K.; Cusworth, D.; O'Neill, K.; Fisk, J.; Thorpe, A.K.; Duren, R. Performance and sensitivity of column-wise and pixel-wise methane retrievals for imaging spectrometers. *Atmos. Meas. Tech.* **2023**, *16*, 6065–6074. [CrossRef]
42. Frankenberg, C.; Platt, U.; Wagner, T. Iterative maximum a posteriori (IMAP)-DOAS for retrieval of strongly absorbing trace gases: Model studies for CH_4 and CO_2 retrieval from near infrared spectra of SCIAMACHY onboard ENVISAT. *Atmos. Chem. Phys.* **2005**, *5*, 9–22. [CrossRef]
43. Thorpe, A.; Frankenberg, C.; Roberts, D. Retrieval techniques for airborne imaging of methane concentrations using high spatial and moderate spectral resolution: Application to AVIRIS. *Atmos. Meas. Tech.* **2014**, *7*, 491–506. [CrossRef]
44. Jiang, Y.; Zhang, L.; Zhang, X.; Cao, X.; Dou, H.; Zhang, L.; Yan, H.; Wang, Y.; Si, Y.; Chen, B. Instrument Performance Analysis for Methane Point Source Retrieval and Estimation Using Remote Sensing Technique. *Remote Sens.* **2025**, *17*, 634. [CrossRef]
45. Ayasse, A.K.; Thorpe, A.K.; Roberts, D.A.; Funk, C.C.; Dennison, P.E.; Frankenberg, C.; Steffke, A.; Aubrey, A.D. Evaluating the effects of surface properties on methane retrievals using a synthetic airborne visible/infrared imaging spectrometer next generation (AVIRIS-NG) image. *Remote Sens. Environ.* **2018**, *215*, 386–397. [CrossRef]
46. Thompson, D.; Leifer, I.; Bovensmann, H.; Eastwood, M.; Fladeland, M.; Frankenberg, C.; Gerilowski, K.; Green, R.; Kratwurst, S.; Krings, T.; et al. Real-time remote detection and measurement for airborne imaging spectroscopy: A case study with methane. *Atmos. Meas. Tech.* **2015**, *8*, 4383–4397. [CrossRef]

47. Foote, M.D.; Dennison, P.E.; Sullivan, P.R.; O'Neill, K.B.; Thorpe, A.K.; Thompson, D.R.; Cusworth, D.H.; Duren, R.; Joshi, S.C. Impact of scene-specific enhancement spectra on matched filter greenhouse gas retrievals from imaging spectroscopy. *Remote Sens. Environ.* **2021**, *264*, 112574. [CrossRef]
48. Pei, Z.; Han, G.; Mao, H.; Chen, C.; Shi, T.; Yang, K.; Ma, X.; Gong, W. Improving quantification of methane point source emissions from imaging spectroscopy. *Remote Sens. Environ.* **2023**, *295*, 113652. [CrossRef]
49. Foote, M.D.; Dennison, P.E.; Thorpe, A.K.; Thompson, D.R.; Jongaramrungruang, S.; Frankenberg, C.; Joshi, S.C. Fast and accurate retrieval of methane concentration from imaging spectrometer data using sparsity prior. *IEEE Trans. Geosci. Remote Sens.* **2020**, *58*, 6480–6492. [CrossRef]
50. Roger, J.; Guanter, L.; Gorroño, J.; Irakulis-Loitxate, I. Exploiting the entire near-infrared spectral range to improve the detection of methane plumes with high-resolution imaging spectrometers. *Atmos. Meas. Tech.* **2024**, *17*, 1333–1346. [CrossRef]
51. Feng, C.; Chen, S.; Zeng, Z.C.; Luo, Y.; Natraj, V.; Yung, Y.L. Aerosol-Calibrated matched filter method for retrievals of methane point source emissions over the Los Angeles Basin. *Earth Space Sci.* **2024**, *11*, e2024EA003519. [CrossRef]
52. Liang, M.; Zhang, Y.; Chen, L.; Tao, J.; Fan, M.; Yu, C. An Effective Quantification of Methane Point-Source Emissions with the Multi-Level Matched Filter from Hyperspectral Imagery. *Remote Sens.* **2025**, *17*, 843. [CrossRef]
53. Li, K.; Bai, K.; Fu, P.; Jiao, P.; Chen, H.; Huang, X.; Liu, C.; Chang, N.B. SSRMF: A sparse spectral reconstruction enhanced matched filter for improving point-source methane emission detection in complex terrain. *ISPRS J. Photogramm. Remote Sens.* **2025**, *225*, 238–256. [CrossRef]
54. Schaum, A. A uniformly most powerful detector of gas plumes against a cluttered background. *Remote Sens. Environ.* **2021**, *260*, 112443. [CrossRef]
55. Bue, B.D.; Lee, J.H.; Brodrick, P.G.; Ruzicka, V.; Fahlen, J.E.; Thorpe, A.K.; Thompson, D.R.; Green, R.O. Suppressing False Enhancements in Spectroscopic Greenhouse Gas Retrievals with the Differential Matched Filter. *EGUsphere* **2026**, *Preprint*. [CrossRef]
56. Xiang, C.; Thompson, D.R.; Green, R.O.; Fahlen, J.E.; Thorpe, A.K.; Brodrick, P.G.; Coleman, R.W.; Lopez, A.M.; Elder, C.D. Identification of false methane plumes for orbital imaging spectrometers: A case study with EMIT. *Remote Sens. Environ.* **2025**, *328*, 114860. [CrossRef]
57. Joyce, P.; Ruiz Villena, C.; Huang, Y.; Webb, A.; Gloor, M.; Wagner, F.H.; Chipperfield, M.P.; Barrio Guilló, R.; Wilson, C.; Boesch, H. Using a deep neural network to detect methane point sources and quantify emissions from PRISMA hyperspectral satellite images. *Atmos. Meas. Tech.* **2023**, *16*, 2627–2640. [CrossRef]
58. Růžička, V.; Mateo-García, G.; Gómez-Chova, L.; Vaughan, A.; Guanter, L.; Markham, A. Semantic Segmentation of Methane Plumes with Hyperspectral Machine Learning Models. *Sci. Rep.* **2023**, *13*, 19999. [CrossRef]
59. Bruno, J.H.; Jervis, D.; Varon, D.J.; Jacob, D.J. U-Plume: Automated Algorithm for Plume Detection and Source Quantification by Satellite Point-Source Imagers. *Atmos. Meas. Tech.* **2024**, *17*, 2625–2644. [CrossRef]
60. Vaughan, A.; Mateo-García, G.; Gómez-Chova, L.; Růžička, V.; Guanter, L.; Irakulis-Loitxate, I. CH4Net: A Deep Learning Model for Monitoring Methane Super-Emitters with Sentinel-2 Imagery. *Atmos. Meas. Tech.* **2024**, *17*, 2583–2593. [CrossRef]
61. Rouet-Leduc, B.; Hulbert, C. Automatic detection of methane emissions in multispectral satellite imagery using a vision transformer. *Nat. Commun.* **2024**, *15*, 3801. [CrossRef]
62. Batchu, V.V.; Conserva, M.; Wilson, A.; Michalak, A.M.; Gulshan, V.; Brodrick, P.G.; Thorpe, A.K.; Van Arsdale, C. Global monitoring of methane point sources using deep learning on hyperspectral radiance measurements from EMIT. *Proc. Natl. Acad. Sci. USA* **2026**, *123*, e2612145123. [CrossRef]
63. Varon, D.J.; Jacob, D.J.; McKeever, J.; Jervis, D.; Durak, B.O.; Xia, Y.; Huang, Y. Quantifying methane point sources from fine-scale satellite observations of atmospheric methane plumes. *Atmos. Meas. Tech.* **2018**, *11*, 5673–5686. [CrossRef]
64. Jacob, D.J.; Varon, D.J.; Cusworth, D.H.; Dennison, P.E.; Frankenberg, C.; Gautam, R.; Guanter, L.; Kelley, J.; McKeever, J.; Ott, L.E.; et al. Quantifying methane emissions from the global scale down to point sources using satellite observations of atmospheric methane. *Atmos. Chem. Phys.* **2022**, *22*, 9617–9646. [CrossRef]
65. Kuhlmann, G.; Koene, E.; Meier, S.; Santaren, D.; Broquet, G.; Chevallier, F.; Hakkarainen, J.; Nurmela, J.; Amorós, L.; Tamminen, J.; et al. The ddeq Python library for point source quantification from remote sensing images (version 1.0). *Geosci. Model Dev.* **2024**, *17*, 4773–4789. [CrossRef]
66. Hakkarainen, J.; Ialongo, I.; Varon, D.J.; Kuhlmann, G.; Krol, M.C. Linear integrated mass enhancement: A method for estimating hotspot emission rates from space-based plume observations. *Remote Sens. Environ.* **2025**, *319*, 114623. [CrossRef]
67. Jongaramrungruang, S.; Thorpe, A.K.; Matheou, G.; Frankenberg, C. MethaNet: An AI-Driven Approach to Quantifying Methane Point-Source Emission from High-Resolution 2-D Plume Imagery. *Remote Sens. Environ.* **2022**, *269*, 112809. [CrossRef]
68. Plewa, T.; Butz, A.; Frankenberg, C.; Thorpe, A.K.; Marshall, J. Improvements of AI-driven emission estimation for point sources applied to high resolution 2-D methane-plume imagery. *Remote Sens. Environ.* **2025**, *331*, 115002. [CrossRef]

69. Ayasse, A.K.; Cusworth, D.H.; Howell, K.; O'Neill, K.; Conrad, B.M.; Johnson, M.R.; Heckler, J.; Asner, G.P.; Duren, R. Probability of detection and multi-sensor persistence of methane emissions from coincident airborne and satellite observations. *Environ. Sci. Technol.* **2024**, *58*, 21536. [CrossRef]
70. Roger, J.; Guanter, L.; Gorroño, J. Assessing the Detection of Methane Plumes in Offshore Areas Using High-Resolution Imaging Spectrometers. *Atmos. Meas. Tech.* **2025**, *18*, 5545–5567. [CrossRef]
71. Zhang, Y.; Gautam, R.; Pandey, S.; Omara, M.; Maasakkers, J.D.; Sadavarte, P.; Lyon, D.; Nesser, H.; Sulprizio, M.P.; Varon, D.J.; et al. Quantifying methane emissions from the largest oil-producing basin in the United States from space. *Sci. Adv.* **2020**, *6*, eaaz5120. [CrossRef]
72. Irakulis-Loitxate, I.; Guanter, L.; Maasakkers, J.D.; Zavala-Araiza, D.; Aben, I. Satellites detect abatable super-emissions in one of the world's largest methane hotspot regions. *Environ. Sci. Technol.* **2022**, *56*, 2143. [CrossRef]
73. Cusworth, D.H.; Duren, R.M.; Thorpe, A.K.; Olson-Duvall, W.; Heckler, J.; Chapman, J.W.; Eastwood, M.L.; Helmlinger, M.C.; Green, R.O.; Asner, G.P.; et al. Intermittency of large methane emitters in the Permian Basin. *Environ. Sci. Technol. Lett.* **2021**, *8*, 567–573. [CrossRef]
74. Yu, J.; Hmiel, B.; Lyon, D.R.; Warren, J.; Cusworth, D.H.; Duren, R.M.; Chen, Y.; Murphy, E.C.; Brandt, A.R. Methane Emissions from Natural Gas Gathering Pipelines in the Permian Basin. *Environ. Sci. Technol. Lett.* **2022**, *9*, 969–974. [CrossRef]
75. Chauhan, A.; Raval, S. Satellite-Derived Approaches for Coal Mine Methane Estimation: A Review. *Remote Sens.* **2025**, *17*, 3652. [CrossRef]
76. Sadavarte, P.; Pandey, S.; Maasakkers, J.D.; Lorente, A.; Borsdorff, T.; Denier van der Gon, H.; Houweling, S.; Aben, I. Methane emissions from superemitting coal mines in Australia quantified using TROPOMI satellite observations. *Environ. Sci. Technol.* **2021**, *55*, 16573–16580. [CrossRef]
77. Peng, S.; Giron, C.; Liu, G.; d'Aspremont, A.; Benoit, A.; Lauvaux, T.; Lin, X.; de Almeida Rodrigues, H.; Saunois, M.; Ciais, P. High-resolution assessment of coal mining methane emissions by satellite in Shanxi, China. *iScience* **2023**, *26*, 108375. [CrossRef]
78. Varon, D.J.; Jacob, D.J.; Jervis, D.; McKeever, J. Quantifying time-averaged methane emissions from individual coal mine vents with GHGSat-D satellite observations. *Environ. Sci. Technol.* **2020**, *54*, 10246–10253. [CrossRef]
79. Maasakkers, J.D.; Varon, D.J.; Elfarsdóttir, A.; McKeever, J.; Jervis, D.; Mahapatra, G.; Pandey, S.; Lorente, A.; Borsdorff, T.; Foorthuis, L.R.; et al. Using satellites to uncover large methane emissions from landfills. *Sci. Adv.* **2022**, *8*, eabn9683. [CrossRef]
80. Cusworth, D.H.; Duren, R.M.; Ayasse, A.K.; Jiorle, R.; Howell, K.; Aubrey, A.; Green, R.O.; Eastwood, M.L.; Chapman, J.W.; Thorpe, A.K.; et al. Quantifying methane emissions from United States landfills. *Science* **2024**, *383*, 1499–1504. [CrossRef]
81. Ayasse, A.K.; Thorpe, A.K.; Cusworth, D.H.; Kort, E.A.; Negron, A.G.; Heckler, J.; Asner, G.; Duren, R.M. Methane remote sensing and emission quantification of offshore shallow water oil and gas platforms in the Gulf of Mexico. *Environ. Res. Lett.* **2022**, *17*, 084039. [CrossRef]
82. Irakulis-Loitxate, I.; Gorroño, J.; Zavala-Araiza, D.; Guanter, L. Satellites detect a methane ultra-emission event from an offshore platform in the Gulf of Mexico. *Environ. Sci. Technol. Lett.* **2022**, *9*, 520–525. [CrossRef]
83. Thompson, D.; Thorpe, A.; Frankenberg, C.; Green, R.; Duren, R.; Guanter, L.; Hollstein, A.; Middleton, E.; Ong, L.; Ungar, S. Space-based remote imaging spectroscopy of the Aliso Canyon CH_4 superemitter. *Geophys. Res. Lett.* **2016**, *43*, 6571–6578. [CrossRef]
84. Conley, S.; Franco, G.; Faloona, I.; Blake, D.R.; Peischl, J.; Ryerson, T. Methane emissions from the 2015 Aliso Canyon blowout in Los Angeles, CA. *Science* **2016**, *351*, 1317–1320. [CrossRef]
85. Cusworth, D.H.; Duren, R.M.; Thorpe, A.K.; Pandey, S.; Maasakkers, J.D.; Aben, I.; Jervis, D.; Varon, D.J.; Jacob, D.J.; Randles, C.A.; et al. Multisatellite imaging of a gas well blowout enables quantification of total methane emissions. *Geophys. Res. Lett.* **2021**, *48*, e2020GL090864. [CrossRef]
86. Guanter, L.; Roger, J.; Sharma, S.; Valverde, A.; Irakulis-Loitxate, I.; Gorroño, J.; Zhang, X.; Schuit, B.J.; Maasakkers, J.D.; Aben, I.; et al. Multisatellite Data Depicts a Record-Breaking Methane Leak from a Well Blowout. *Environ. Sci. Technol. Lett.* **2024**, *11*, 825–830. [CrossRef]
87. United Nations Environment Programme. Methane Alert and Response System (MARS), 2026. Official Website. Available online: https://www.unep.org/en/what-we-do/energy/methane/methane-alert-and-response-system-mars (accessed on 1 November 2026).

Disclaimer/Publisher's Note: The statements, opinions and data contained in all publications are solely those of the individual author(s) and contributor(s) and not of MDPI and/or the editor(s). MDPI and/or the editor(s) disclaim responsibility for any injury to people or property resulting from any ideas, methods, instructions or products referred to in the content.